Title

Influence of microchannel geometry on device performance and electrophysiological recording fidelity during long-term studies of connected neural populations

Journal

Lab on a Chip, 22(20)

ISSN

1473-0197

Authors

Goshi, Noah
Girardi, Gregory
da Costa Souza, Felipe
et al.

Publication Date

2022-10-11

DOI

10.1039/d2lc00683a

Peer reviewed

Lab on a Chip

ROYAL SOCIETY OF CHEMISTRY

PAPER

View Article Online
View Journal

Cite this: DOI: 10.1039/d2lc00683a

Influence of microchannel geometry on device performance and electrophysiological recording fidelity during long-term studies of connected neural populations†

Noah Goshi,[a] Gregory Girardi,[a] Felipe da Costa Souza,[b] Alexander Gardner,[c] Pamela J. Lein[b] and Erkin Seker *[c]

Received 23rd July 2022,
Accepted 12th September 2022

DOI: 10.1039/d2lc00683a

rsc.li/loc

Compartmentalized microfluidic neural cell culture platforms, which physically separate axons from the neural soma using a series of microchannels, have been used for studying a wide range of pathological conditions and basic neuroscience questions. While each study has different experimental needs, the fundamental design of these devices has largely remained unchanged and a systematic study to establish long-term neural cultures in this format is lacking. Here, we investigate the influence of microchannel geometry and cell seeding density on device performance particularly in the context of long-term studies of synaptically-connected, yet fluidically-isolated neural populations of neurons and glia. Of the different experimental parameters, the microchannel height was the principal determinant of device performance, where the other parameters offer additional degrees of freedom in customizing such devices for specific applications. We condense the effects of these parameters into design rules and demonstrate their utility in engineering a microfluidic neural culture platform with integrated microelectrode arrays. The engineered device successfully recorded from primary rat cortical cells for 59 days *in vitro* with more than on order of magnitude enhancement in signal-to-noise ratio in the microchannels.

Introduction

The central nervous system (CNS) is extremely complex, with each neuron communicating with hundreds to thousands of other neurons *via* synaptic connections.[1] In addition, glial cells are in constant contact with neurons, and any disruption or dysregulation within this highly interconnected system can lead to disease states. This high complexity and interconnectivity has led to disproportionally high failure rates of late phase clinical trials targeting neurological disorders.[2] One common approach to overcome this challenge has been the development of organ-on-a-chip models with electrophysiological read-out capabilities,[3] which can be used to gain a better understanding of specific cellular and molecular mechanisms behind many neurological and neurodegenerative diseases. These models aim to reduce the complexity of the system as compared to *in vivo* models, while still maintaining many of the critical characteristics of the *in vivo* microenvironment (*e.g.*, presence of relevant glial cells, mature neuronal networks, and distinct neural populations), and thereby allow researchers to conduct highly directed cellular level experiments with increased physiological relevance.

One popular example of an organ-on-a-chip model to study the CNS was first described by Taylor *et al.*,[4] and involves the use of polydimethylsiloxane (PDMS) based microfluidic culture platforms to physically separate the cell bodies of neurons and their axons. These culture platforms consist of two large cell culture chambers (which house the cell somas) and are connected by an array of microchannels that, due to their reduced height, only allow neurites to pass through. Additionally, fluidic isolation of one chamber (primary) can be achieved by increasing the volume of media in the opposing chamber (secondary), thereby driving a hydrostatic pressure driven flow through the microchannels counteracting any diffusion from the primary chamber to the secondary chamber. These devices were initially used to study isolated axons, along with their growth and regeneration following injury.[5] Researchers have subsequently adapted the original design for use in myriads of other studies including

[a] *Department of Biomedical Engineering, University of California – Davis, Davis, CA 95616, USA*
[b] *Department of Molecular Biosciences, University of California – Davis, Davis, CA 95616, USA*
[c] *Department of Electrical and Computer Engineering, University of California – Davis, Davis, CA 95616, USA. E-mail: eseker@ucdavis.edu*

† Electronic supplementary information (ESI) available. See DOI: https://doi.org/10.1039/d2lc00683a

the formation of directional neural networks,[6–8] investigating the transport and propagation of neurodegenerative disease related proteins,[9–14] studying the spread of glutamate-induced ecotoxicity,[15] and the innervation of non-neuronal cell cultures.[16,17] While many great insights have been gained from these studies, the fundamental design of the platform – in particular the geometry interconnecting microchannel array – has largely been unchanged and may not be suitable for every application, especially for chronic studies that are necessary for recapitulating mature neuronal networks.

We performed a meta-analysis of over 200 unique research articles using similar organ-on-a-chip devices and found that ~70% articles used devices with geometries identical to the original devices described by Taylor *et al.*,[4,5] irrespective of cell type (CNS *vs.* PNS), presence of glial cells, and experimental objective (Fig. S1†). Additionally, for the studies that used microchannels with different dimensions, nearly all of them used devices with larger microchannels, and in general there was limited discussion regarding the change over the common microchannel dimension. In the original device, the microchannels were 3 μm × 8–10 μm (height × width), with lengths ranging from 150–900 μm.[4,5] The small height of the microchannels was largely effective at preventing the soma of the neurons (with average diameter's ranging between 7–58 μm)[18] from entering the microchannels, while allowing axons and dendrites (with diameters ranging between 0.2–2.2 μm)[18,19] to easily enter and traverse the channels. The range of lengths were used to differentiate axons from dendrites, as it was noted that dendrites were unable to fully pass through microchannels greater than 450 μm in length.[5] Taken together, the meta-analysis suggests that the majority of researchers use the original device dimensions, and the reasons for using a specific channel dimensions are not often discussed, even though these dimensions likely play a significant role in the device function.

In this paper we investigate the influence of microchannel geometry on device performance particularly in the context of long-term studies (1+ month) of synaptically-connected yet fluidically-isolated neural populations. Compared to acute studies, maintaining fluidic isolation becomes much more challenging as the fluid flow through the microchannels that counteracts diffusion is no longer negligible and may significantly alter the concentration of effector molecules. Additionally, for long-term studies, the inclusion of glial cells in the neuronal culture has been shown to improve the overall health of the culture and neuron function.[20,21] Of the different glial cells that are included in these mixed cultures, astrocytes, which contain fine processes with similar diameters to axons,[22] are able to extend processes a significant distance into the microchannels, which may confound experimental results. Here, we cultured primary rat cortical neurons and astrocytes in microfluidic culture platforms with varying microchannel dimensions to systematically compare the influence of microchannel dimensions and initial seeding densities, on the fluidic properties of the platform and the ability for neurons, astrocytes, and nuclei to enter and cross through the microchannels. In addition, we study the influence of microchannel geometry on the electrophysiological recording fidelity. We demonstrate that microchannel height has an outstanding impact on the fluidic properties of the platform, while the seeding density can be used to adjust the number of astrocyte processes entering the microchannels. Using this information, we designed platforms that enable chronic studies, and demonstrate that neural activity can be recorded from these platforms (from electrodes placed under the cell culture chambers and microchannels) for at least 59 days *in vitro* (DIV) with more than an order of magnitude enhancement in signal-to-noise ratio in microchannels and significantly higher number of active electrodes. This study demonstrates the importance that small changes in microchannel dimensions can have on the overall performance of commonly-used microfluidic neural cell culture platforms and concludes with considerations for designing similar organ-on-a-chip devices for long-term neural culture and electrophysiology.

Experimental

Microfluidic platform design and fabrication

Multiple microchannel platforms were designed in order to assess the influence of microchannel geometry on different properties of the device (Fig. 1A). "Array" style devices were designed to investigate the cellular response to different microchannel geometries. Each array device contained 4, 25 microchannel arrays with widths of 2, 5, 10, and 15 μm. Additionally, these devices were designed with microchannel

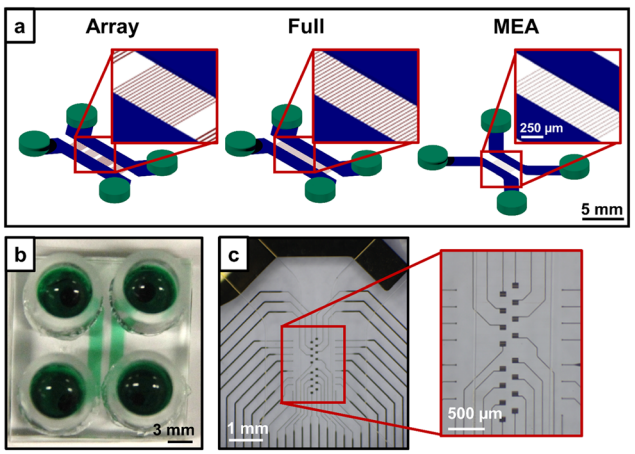

Fig. 1 Examples of different microfluidic platforms used in this study. (a) 3D renderings of the three styles of microfluidic platforms. The microchannels are shown in red with dimensions of 1.5–6 μm × 2–15 μm × 500–1500 μm (height × width × length) depending on the design. The cell culture chambers are shown in blue with a height of 75 μm. The fluidic access ports are shown in green and created *via* biopsy punch (3 mm Ø) over which glass cloning cylinders (6 mm Ø, 8 mm height) were affixed to increase the overall media volume capacity. (b) An example of a fully assembled device with affixed cloning cylinders. (c) An example of an "MEA" style device with the integrated MEA.

lengths of 500, 1000, and 1500 μm and heights of 1.5, 3, and 6 μm. "Full" style devices were used to determine the influence of microchannel geometries (of a single channel width per device) on the fluidic properties of the devices. These devices each had 101 microchannels with dimensions of 10 μm × 1000 μm × 1.5 or 6 μm (width × length × height). Finally, "MEA" style devices contained an array of 25 microchannels with dimensions of 5 or 10 μm × 1000 μm × 1.5 μm (width × length × height), which were bonded over custom microelectrode arrays (MEAs) designed for integration into the microchannel devices.

The fabrication of the microfluidic platforms followed standard soft lithography techniques. Briefly, master molds containing the different platform geometries were fabricated by patterning two layers of SU-8 (Kayaku Advanced Materials) on a silicon wafer using standard photolithography techniques. The first layer defined the interconnecting microchannels and was fabricated using SU-8 6005 deposited with different spin rates to achieve a final thickness of 1.5, 3, or 6 μm. The second layer defined the cell culture chambers and was fabricated using SU-8 2050 with a final thickness of 75 μm. Following the patterning of the cell culture chamber layer, the master molds were hard-baked for 1 h at 250 °C. All dimensions of the microfluidic platform master molds were confirmed using a Bruker Dektak XT profilometer following the hard-bake.

The master molds were placed in a 100 mm-diameter (Ø) Petri dish and premixed (1 : 10 w/w curing agent to base) polydimethylsiloxane (PDMS; Sylgard 184, Dow Corning) was poured over the mold and placed in a vacuum chamber to remove any bubbles. The PDMS was then placed on a 90 °C hotplate for 2.5 h to cure. The PDMS platforms were removed from the master mold and fluidic ports to access the cell culture chambers were opened using a 3 mm Ø biopsy punch. For the "array" and "full" style devices, the PDMS platforms were reversibly bonded to poly-L-lysine (PLL) coated glass coverslips. PLL coating was done by incubating the 0.5 mg mL^{-1} PLL (Sigma) in B-buffer (3.1 mg mL^{-1} boric acid and 4.75 mg mL^{-1} borax, Sigma) for 4 h at 37 °C and 5% CO_2. The coverslips were then washed with sterile deionized (DI) water and air dried. To produce reversibly bonded devices, the PDMS platforms were sterilized with 70% EtOH followed by treatment in an air plasma cleaner at 10 W for 2 min. The PDMS platforms were then sealed over the PLL coated glass coverslips and glass cloning cylinders (8 mm × 6 mm inner Ø, Sigma) were fixed over each of the fluidic ports using sterile vacuum grease (Dow Corning) to form the final device (Fig. 1B).

Custom MEAs were designed and fabricated to be integrated into "MEA" style devices (Fig. 1C). Each MEA contained an array of 8 microelectrodes in each cell culture chamber, and an array of 16 microelectrodes placed under the microchannels, with microelectrodes having a surface area of 400 μm^2. The electrodes and traces (250 nm-thick Au over a 160 nm-thick Cr adhesion layer) were sputter-deposited on borosilicate glass wafers (500 μm thick, University Wafers) and patterned using standard lift-off techniques. A 250 nm layer of SiO_2 was deposited *via* PECVD to serve as the insulation layer. Finally, the electrode sites were lithographically patterned and opened *via* a brief immersion in buffered oxide etch. To form the final integrated microfluidic device, the MEAs were treated with air plasma to be permanently bonded to the corresponding "MEA" style microfluidic platform. Both the MEA and PDMS platforms were sterilized with 70% EtOH and the surfaces were activated with air plasma at 10 W for 2 min. The MEA was then covered with 70% EtOH and the PDMS platform was placed over the MEA and aligned under a microscope. The aligned device was placed in a vacuum chamber for 1 h to remove the EtOH solution and permanently bond the MEA and PDMS platform. The bonded devices were then treated with air plasma at 30 W for 10 min to make the surfaces hydrophilic and glass cloning cylinders were fixed over the fluidic ports. Finally, PLL solution was added to the device and incubated for 4 h and washed with sterile DI water to coat the interior surfaces of the device.

Analytical and computational modelling of fluid flow

Analytical modeling of the fluidic properties of the devices was done using previously described electrical circuit analogies, treating the interconnecting microchannels as resistors and the open wells containing media as capacitors.[23] The dimensions of the model were the same as the "full" device with 101 microchannels with widths of 10 μm and lengths of 1000 μm. An initial volume differential of 150 μL per cell chamber (75 μL per well) was used to drive the hydrostatic pressure-induced flow, which amounted to a height differential of ~2.65 mm using the 6 mm inner Ø of the cloning cylinders. Computational modeling was done using COMSOL Multiphysics 5.5 solving for the Navier–Stokes equations to model the pressure-driven flow through the microchannels in a 3D model of the "full" device. The volumetric flow rate through the microchannels was determined at steady state with an initial pressure differential corresponding to a volume differential of 150 μL across the chambers. Detailed descriptions of the analytical and computational models can be found in the ESI.†

Primary cortical culture

All procedures involving animals were conducted in accordance with the National Institutes of Health Guide for the Care and Use of Laboratory Animals following protocols approved by the University of California, Davis Institutional Animal Care and Use Committee. Timed-pregnant Sprague–Dawley rats were purchased from Charles River Laboratory (Hollister, CA). All animals were housed in clear plastic shoebox cages containing corn cob bedding under constant temperature (22 ± 2 °C) and 12 h light–dark cycle. Food and water were provided *ad libitum*. Primary cortical cultures were prepared from postnatal day 0 rat pups as previously

described.[24] Neocortices from all pups in the litter were pooled and dissociated.

Prior to seeding PLL coated devices were covered with plating medium (PM) consisting of Neurobasal A culture medium supplemented with 2% B27 supplement, 1X GlutaMAX, 10% heat-inactivated horse serum, and 20 mM HEPES at pH 7.5 (all from ThermoFisher). Primary cortical cells were seeded in PM at a density of 3×10^6–20×10^6 cells per mL by adding 20 μL of the cell suspension to the upper well of each chamber and incubated at 37 °C for 4 h to allow the cells to flow into the chamber and adhere. For experiments quantifying the cellular response to microchannel geometry, only one chamber was seeded with cells, and the other chamber was loaded with 20 μL of PM. Following the incubation, the excess PM and unattached cells were removed, and each well was filled with 150 μL of growth medium (GM) consisting of Neurobasal A culture medium supplemented with 2% B27, 1X GlutaMAX (all from ThermoFisher). Half media changes were performed twice a week throughout the length of the experiments.

Immunocytochemistry

At the conclusion of the experiment, cell cultures were washed 3 times with 37 °C DPBS with calcium and magnesium (DPBS+) and fixed using 4% w/v paraformaldehyde (PFA; Affymetrix) in PBS for 2.5 h. For reversibly bonded devices, the PDMS overlay was removed and the glass coverslip with the fixed cells was washed 3 times with DPBS+ to remove any residual PFA. For permanently bonded devices, following fixation, the PFA was removed, and the devices were washed 3 times with DPBS+.

For reversibly bonded devices, the fixed cells were washed twice with 0.05% v/v Tween20 (Sigma) solution in DPBS+, followed by a 3 min permeabilization with 0.1% v/v Triton X-100 (ThermoFisher) solution in DPBS+ and two additional washes with Tween20/ DPBS+ solution. Samples were blocked with a solution of 0.5% v/v heat-inactivated goat serum (ThermoFisher) and 0.3 M glycine (Sigma) in DPBS+ (blocking buffer) for 1 h. Following the blocking step, samples were incubated for 1 h in primary antibody solution containing anti-βIII tubulin (ThermoFisher) and rabbit anti-GFAP (ThermoFisher) in blocking buffer. Samples were then washed 3 times with Tween20 solution before a 1 h incubation with secondary antibody solution containing goat anti-mouse antibodies conjugated to AlexaFluor 647 (ThermoFisher) and goat anti-rabbit antibodies conjugated to AlexaFluor 488 (ThermoFisher). Following incubation with secondary antibody solution, the samples were washed 3 times with DPBS+. Lastly, samples were incubated for 5 min with a 4′,6-diamidino-2-phenylindole (DAPI) solution (1 : 20000 dilution in DI H_2O, Sigma), followed by an additional Tween20 solution wash before mounting onto glass slides using ProLong Gold Antifade Mountant (ThermoFisher).

For the permanently bonded devices, a similar methodology was followed, with increased incubation durations to ensure permeation of the reagents into the microchannels: (i) the permeabilization step was done with Tween20 solution with a 4 h incubation, (ii) the blocking step increased to an overnight incubation (18 h) at 4 °C, and (iii) the primary and secondary antibody incubation steps each increased to 72 h at 4 °C.

Quantification of cell culture response to microchannel geometry

To quantify the cellular response, primary cortical cells were cultured for 14 days in one chamber of the "array" style device and fixed and immunostained as described above. All sample images were acquired with a Zeiss Observer D1 inverted fluorescence microscope at 100× magnification and analyzed with ImageJ. Four different responses were quantified by manually determining: (i) the number of microchannels with at least 1 axon crossing the entire length of the channel, (ii) the number of nuclei that entered or crossed through the microchannels, (iii) the number of channels that had at least 1 astrocyte process entering the channel, (iv) the length that the astrocyte process extended into the microchannels (Fig. 2).

Electrophysiology recording and analysis

For electrophysiology measurements, the devices were placed on a custom-built rig and maintained at 37 °C and 5% CO_2 during the recordings. Recordings were performed at a sampling frequency of 30 kHz using an RHD2132 Intan amplifier (Intan Technologies). Half-media changes were performed 24 h prior to each recording.

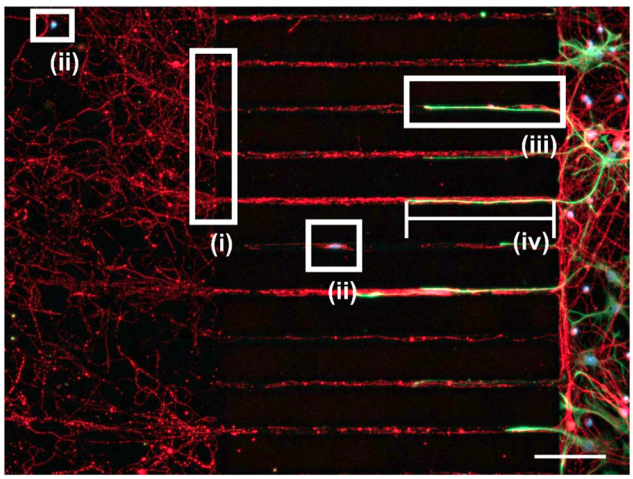

Fig. 2 Representative fluorescence image illustrating the different cellular responses to varying device parameters. The cultures were immunostained for neurons – anti-βIII-tubulin (red) and astrocytes – anti-GFAP (green) and the general nuclear stain DAPI (blue). The responses quantified are as follows: (i) the number of microchannels with at least 1 axon crossing the entire length of the channel, (ii) the number of nuclei that entered or crossed through the microchannels, (iii) the number of channels that had at least 1 astrocyte process entering the channel, (iv) the length that the astrocyte process extended into the microchannels. Scale bar = 100 μm.

Feature extraction from the recordings was done using Offline Sorter and NeuroExplorer (Plexon). Spikes were detected following a filtering (300 Hz high pass) using a threshold of 8× standard deviation of the noise. Channels that showed less than 10 spikes per 10 min recording were discarded from the analysis. The number of active electrodes for each array (or electrode position – *i.e.*, placed under a 5 μm wide channel, 10 μm wide channel, or within the culture chamber) was determined as the number of electrodes with at least 10 spikes detected during the 10 min recording. Overall synchrony of the active electrodes within each device was determined using the SPIKE-distance methodology[25] using the PySpike Python package.[26] The following features were determined on a per electrode basis, but statistical analysis was performed on a per device basis by taking the overall mean from the active electrodes. The signal-to-noise ratio (SNR) and root mean (RMS) noise from each active electrode were automatically determined by Offline Sorter. Bursts were classified using the *max interval* method in NeuroExplorer using previously defined parameters.[21,27] Briefly these parameters were; (i) maximum initial inter-spike interval (ISI) of 0.1 s, (ii) maximum end ISI of 0.25 s, (iii) minimum inter-burst interval of 0.8 s, (iv) minimum burst duration of 0.05 s, and (v) minimum number of spikes in bursts of 6 spikes. The percentage of total spikes within bursts, the average burst duration, and average ISI within bursts were also calculated at a per electrode basis.

Statistical analysis

Hierarchical linear regression was used to determine the most impactful predictor variables (3 microchannel dimensions and seeding density) on each of the 4 cellular responses. As all the predictor variables and responses showed a non-Gaussian distribution, each was normalized prior to employing a forward stepwise linear regression analysis. To compare change in the different spike features based on electrode position, each data set was fitted using a linear mixed effects model (treating the individual devices as a random effect) with a b-spline basis to account for the overall shape of the plots. We then compared the estimated marginal means from the fitted curves at 3 pre-determined timepoints (7, 21, and 56 DIV) representing the early, middle, and late stages of the cultures and adjusted for multiple comparisons using Tukey's method. In all cases a p-value $<$ 0.05 was considered significant. All statistical analyses were performed in R.

Results and discussion

Cell culture response to different microchannel dimensions

In order to improve the long-term performance of microfluidic cell culture platforms that were used to study synaptically connected neural populations, we compared the response of the primary cortical cells cultured in "array" style devices to a number of different variables including microchannel width, length, and height along with the initial seeding density. One chamber of the device was seeded with 20 μL of cortical cells at high (20×10^6 cells per mL) and low (3×10^6 cells per mL) concentrations. A seeding volume of 20 μL was chosen as preliminary studies indicated that higher seeding volumes lead to a more even distribution of cells within the chamber, without altering the plating density. Nevertheless, multiple designs of each "array" style device were fabricated, in which the order of arrays of microchannels were randomly placed along the device to account for any uneven distribution of seeding density. The cortical cells in these devices were maintained for 14 DIV, after which they were fixed, and the different culture responses were quantified.

Axon crossing microchannels. One critical parameter determining the functionality of these organ-on-a-chip devices is the ability for axons to cross through the microchannels and thereby synaptically connect the two neural populations. Our results indicate that for most microchannel geometries, by DIV 14 axons are able to consistently cross through all available microchannels, especially at higher seeding densities (Fig. 3a). However, we observe a clear reduction in the number of microchannels with axon crossings at small channel widths (2 μm) and long channel lengths (1500 μm), which is exacerbated at low seeding densities. These observations were confirmed by hierarchical regression analysis (Fig. 4a), which indicates that the most significant variables, in order of importance, were seeding density, microchannel width, and microchannel length. Interestingly, microchannel height, while still significantly improving the adjusted R^2 coefficient of the regression model, had the least impact on the ability for axons to cross through the microchannels (Fig. 3a and 4a). It has been shown that axons from cortical neurons have heights of less than 1 μm when cultured on planar surfaces,[28] and therefore axons were not physically excluded from the microchannels even at the lowest tested height. Additionally, while percentage of microchannels with at least one axon crossing did not substantially increase as microchannel widths increased above 5 μm, we did observe that microchannels with increased widths had a larger number of axons crossing through each individual microchannel.

Soma confinement in chambers. The ability to effectively confine the somas from each cell population to their respective chamber is another critical aspect to the effectiveness of these devices. Although the height of the most reported microchannel geometries are smaller than the size of neurons and glial cells (Fig. S1†), there are a number of reports of showing significant populations of neurons or glial cells that pass through similarly designed microchannels.[29–32] We found that microchannel height had a significant impact on the soma confinement capabilities of the device (Fig. 3b) and was the most significant factor in explaining the observed variance (Fig. 4b). Additionally, increasing the seeding density ubiquitously increased the number of non-confined cells across all conditions, and was the second most important factor identified by hierarchical regression analysis (Fig. 3b and 4b). For devices seeded at 20 ×

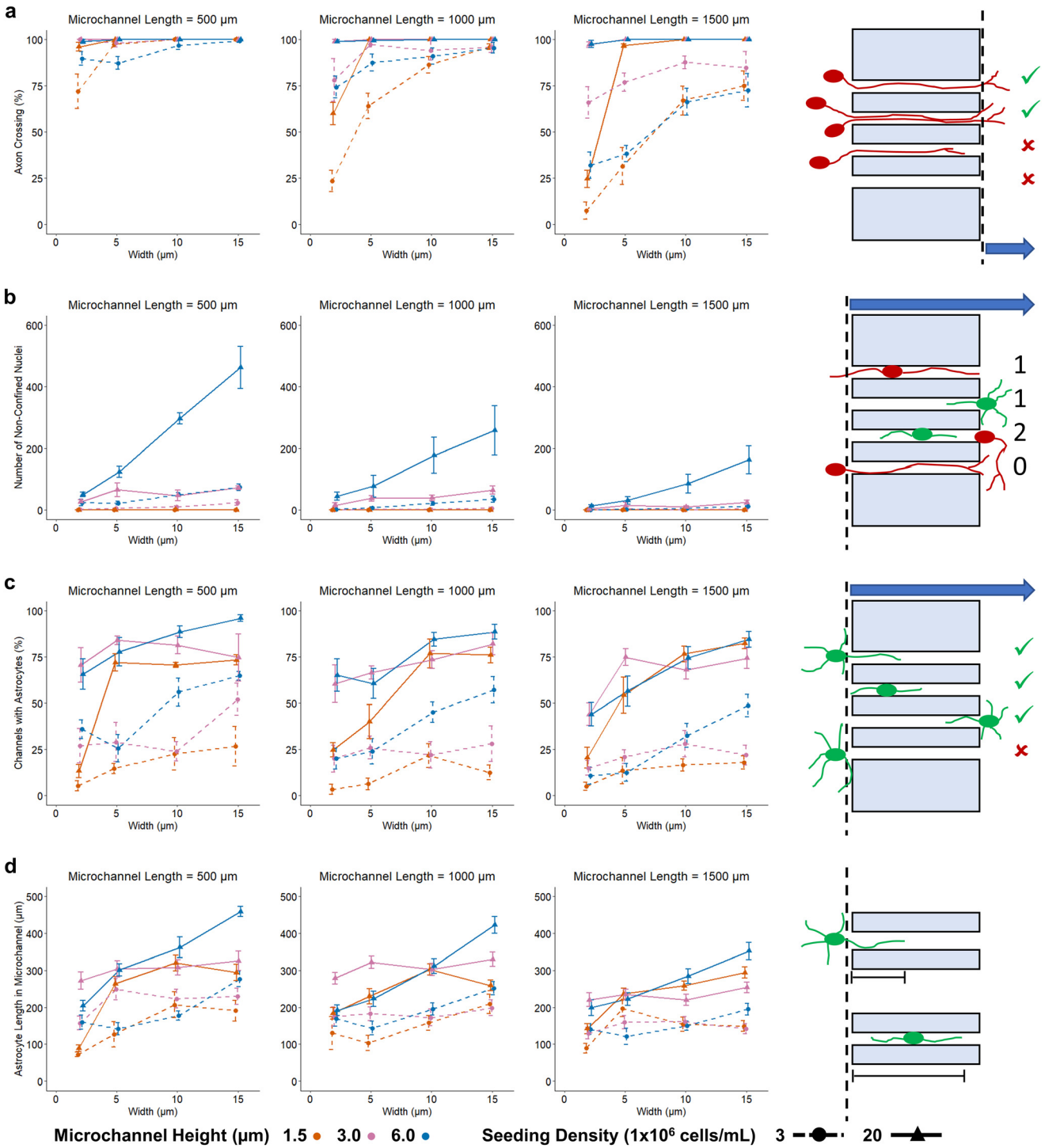

Fig. 3 Quantification of (a) the percentage of microchannels with at least one axon crossing the entirety of the channel, (b) the number of non-confined cell bodies (nuclei), (c) the percentage of microchannels that contained at least one astrocyte process, and (d) the length that the astrocyte process extended into the microchannels to varying device parameters (mean ± SEM, n = 4–8 from two independent dissections). For the quantification of astrocyte length, only channels that contained at least one astrocyte process were analyzed. A schematic representation of how each response was quantified is shown in the right-most column.

10^6 cells per mL the number of non-confined cells averaged across all microchannel widths and lengths, were 0.25 ± 0.65, 31.78 ± 30.28, and 145.36 ± 161.93 for devices with microchannel heights of 1.5, 3, and 6 µm respectively. These values dropped to 0.21 ± 0.44, 4.28 ± 7.29, and 19.29 ± 24.20 when the initial seeding density was reduced to 3×10^6 cells per mL. Microchannel width and length also played a significant role in determining the effectiveness of the cellular confinement

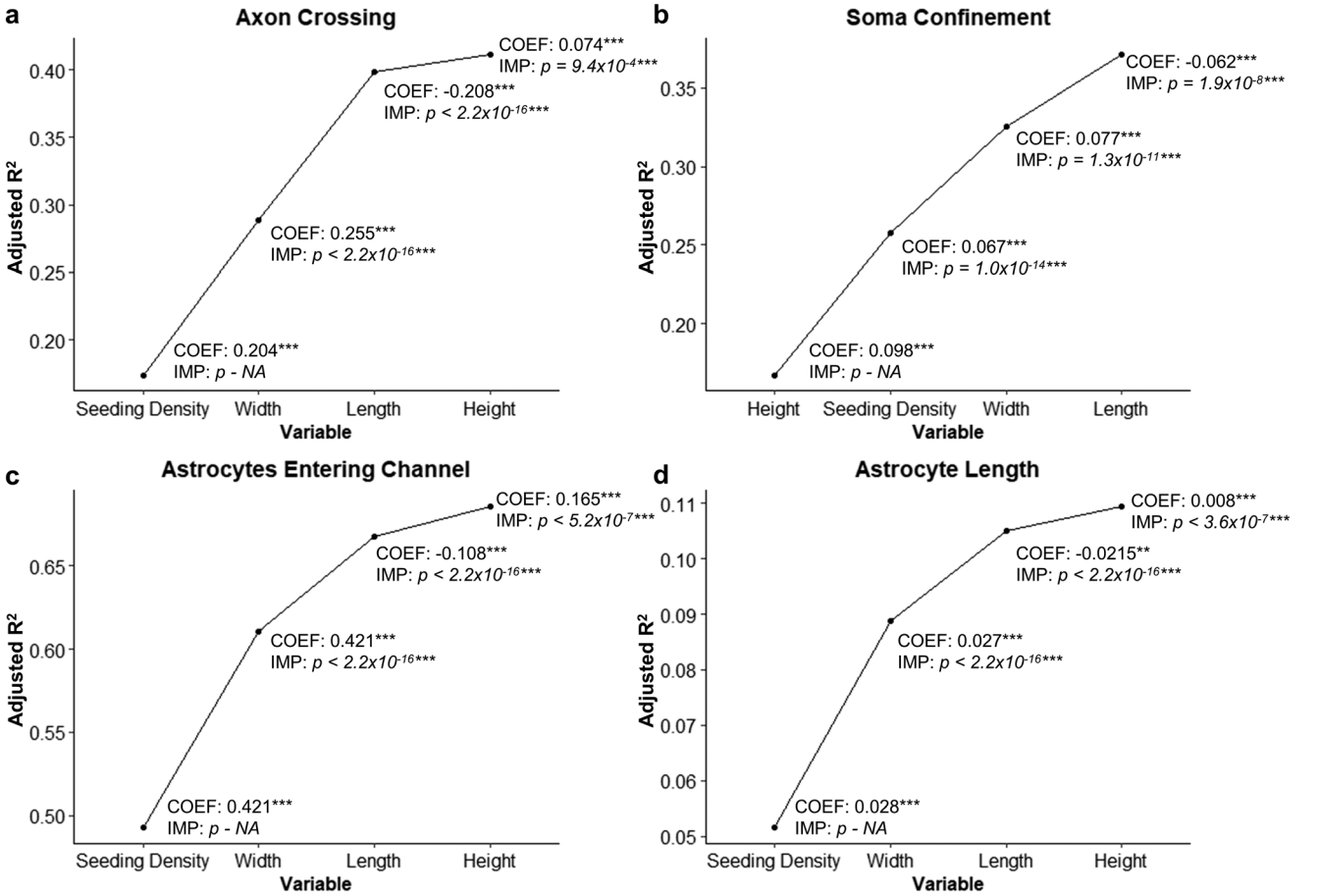

Fig. 4 Plots showing the change in the adjusted R^2 following the addition of each variable in the stepwise linear regression model for (a) the percentage of microchannels with at least one axon crossing fully through the microchannel, (b) the number of nuclei not confined to the initial seeding chamber, (c) the number of microchannels with at least one astrocyte process in them, and (d) the length that the astrocyte process extended into a microchannel. IMP indicates the p-value for the improvement in adjusted R^2 due to the addition of the respective variable. COEF indicates the coefficient of that variable in the full model with all four variables included. $^*p < 0.05$, $^{**}p < 0.01$, $^{***}p < 0.001$.

of the devices, but their effect was only observed at larger channel heights and higher seeding densities (Fig. 3b and 4b).

Interestingly, while we initially expected to see similar numbers of cells entering or crossing through the microchannels with similar cross-sectional areas (*i.e.*, 5 μm wide × 6 μm tall *vs.* 10 μm wide × 3 μm tall), we observed that microchannel height plays a substantially greater role in determining if cell nuclei can enter the microchannels. Microchannels with heights of 1.5 μm showed a near complete confinement of nuclei within the seeded cell culture chamber, regardless of seeding density or other microchannel dimensions. It has been shown that nuclei in cultured cells can undergo large deformations in width and length to pass through confined microchannels but show a lesser ability to adjust nuclei height.[33] It has also been shown that compressing the nuclei of HeLa cells below 3.5 μm leads to nuclear lamina rupture, nuclear blebbing, and alterations in gene expression.[34] This suggests that for these devices, reducing microchannel heights below 3 μm may be an effective way to ensure near total confinement of cells within their seeded chambers. Additionally, we observed that the loss of somal confinement occurred rapidly following cell seeding, most likely due to cells flowing into the channels during the initial seeding. This observation is supported by comparing the overall ratio of neurons to astrocytes that were not confined to the seeded cell chamber. Averaged across all conditions, the ratio of neurons to total cells was 0.92 ± 0.08. While it has been shown that small populations of cultured neurons can migrate in response to specific stimuli, the large majority of cultured neurons are considered non-motile.[35,36] Conversely, astrocytes have been shown to migrate readily even in the absence of stimulation,[37] and therefore we would expect a higher ratio of non-confined astrocytes to neurons if post-seeding migration was dominant. This suggests that cell confinement may not be a critical factor if each chamber is seeded with cells from the same initial population, however in instances where two distinct cell populations are seeded in opposing chambers, reducing microchannel height to prevent cellular cross-contamination is critical.

Astrocytes permeating microchannels. Many studies have demonstrated that culturing neurons with other glial cells can improve the overall health of the neuronal cultures

especially at later timepoints (>28 DIV).[20,21,38] Previous studies along with our own preliminary experiments indicated that microglia, mature oligodendrocytes (OLs), and oligodendrocyte precursor cells (OPCs) do not interact significantly with the microchannels,[39–41] however astrocytes are able to extend processes significant distances into the microchannels. Therefore, we wanted to quantify the astrocyte response to different microchannel geometries. We observed that seeding density was the primary factor in determining the percentage of microchannels containing at least one astrocyte process (Fig. 3c and 4c), accounting for nearly 50% of the variance. As astrocytes account for only ~20% of the cells seeded, it is unsurprising that increasing the number of astrocytes close to the microchannels has the largest effect. The addition of microchannel width, length, and height to the regression model each improves the adjusted R^2 value of the model by a statistically significant amount (Fig. 4c), where microchannel height had the least impact on the ability for astrocyte processes to enter the channel. Similar to axons, this is most likely due to the fact that cultured astrocytes have an average height of less than 1 μm,[22] and therefore would largely be unaffected by the reduction in channel height. All four parameters significantly influenced the length that astrocyte processes extended into the microchannel, but compared to the other culture responses, the proportion of the variance explained by these four parameters was substantially less (adj R^2 for the full model = 0.11) (Fig. 4d). However, we observed that astrocytes were able to extend processes up to ~450 μm into the microchannels with the largest cross-sectional areas (6 μm × 15 μm). This suggests that when co-culturing neurons and astrocytes together in these devices, microchannel lengths should be a minimum of 1000 μm to prevent the formation of astrocyte-astrocyte gap junctions, which may confound experimental results that assume only synaptic connectivity between the chambers.

Influence of microchannel height on the stability of soluble factor concentrations in the chambers

In addition to the cellular response, the fluidic properties of these microfluidic neural culture platforms can be significantly altered by small changes in microchannel geometry. While many papers using these devices highlight and employ the fluidic isolation capabilities of these devices, the volume of fluid flow between the cell culture chambers required to counteract diffusion and maintain fluidic isolation is less studied. While at short time scales (minutes to hours), effects of this fluid flow are negligible, at longer timescales (days to weeks) this fluid flow may significantly alter the concentration of soluble factors (*e.g.*, pharmaceuticals) added to the fluidically isolated chamber. In order to study this, we estimated the fluid flow through the microchannels using an electric circuit analog. We determined that of the three microchannel dimensions, microchannel height had the largest influence on the estimated fluid flow. This is largely due to the cubic relationship between the height of a rectangular microchannel and its hydraulic resistance. Table 1 shows the estimated volumetric flow rate through "full" style devices (10 μm width × 1000 μm length, with 101 microchannels) with varying heights and an initial volume differential of 75 μL per well or ~2.65 mm difference in height. When the microchannel height was increased to 5 μm, ~18 μL flowed between the chambers within only 24 h. While this volume appears negligible, the volume of each cell culture chamber of the full device is ~2.45 μL, resulting in the entire volume of the cell culture chamber being overturned every ~3.25 hours. We also estimated the volumetric flow rate through the microchannels using a 3D computational model of the "full" style device using COMSOL Multiphysics 5.5 (Table 1). The COMSOL simulation showed a good agreement with the electrical circuit analogy. The higher values estimated by the COMSOL model can be attributed to the fact that the COMSOL model was solved for steady-state, and thus the pressure between the chambers did not decrease with the change in volume differential.

Table 1 Estimated volumetric flow rate for the first 24 h given by electrical circuit analogy or 3D computational model (COMSOL)

Channel height (μm)	Q (μL per day) circuit analogy	Q (μL per day) COMSOL
1	0.20	0.20
2	1.48	1.57
5	18.19	22.58

In order to experimentally confirm the results from the electric circuit analog and computational model, that is, whether dilution of the treatment chamber soluble factors is significant due to the media flow, we seeded primary cortical cells at a density of 3×10^6 cells per mL in both cell culture chamber of "full" style devices with microchannel heights of 1.5 μm and 6 μm. After allowing the cells to adhere, 150 μL of GM was added to each well connected to the "secondary" chamber, while 75 μL GM with 50 μM cytosine arabinoside (AraC) was added to each well connected to the "treatment" chamber. The devices were maintained for 48 h with no media changes, after which they were fixed and immunostained. At this concentration AraC acts as a neurotoxic factor,[42] and thus we would expect to see significant neural death in the treatment chambers. As expected, we observed significant neural death in the treatment chamber of microfluidic platforms with microchannel heights of 1.5 μm, however we did not see any neural death in the treatment chambers of the devices with microchannel heights of 6 μm (Fig. 5a). In order to quantify neuronal cell viability, we compared the percent area of each field-of-view stained for β-III tubulin with a circularity less than 0.2 using ImageJ (Fig. 5b). The circularity cutoff was used to eliminate the contribution of cell debris from apoptotic/necrotic neurons, which still stained for β-III tubulin, but lacked long cellular processes, and therefore had high circularity values. A two-way ANOVA indicated a significant interaction between

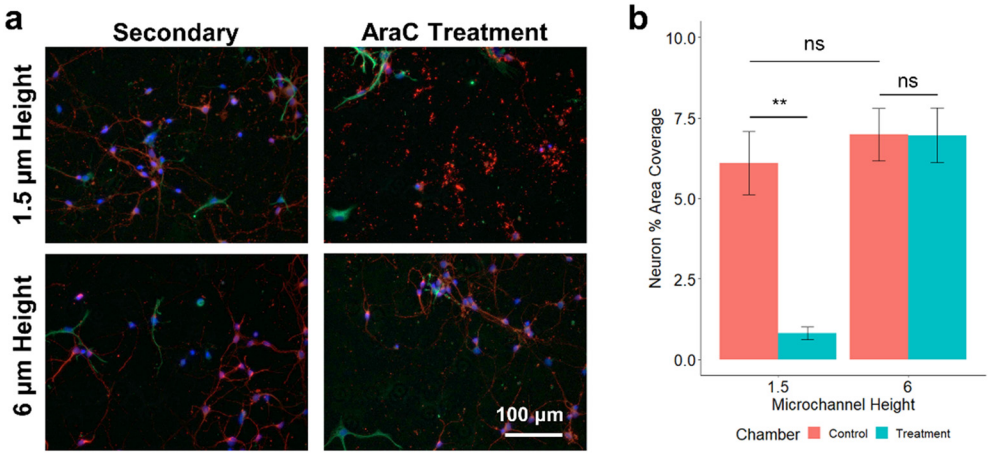

Fig. 5 (a) Representative fluorescence images from the different cell culture chambers following 48 h exposure to 50 μM AraC in the treatment chamber. The cultures were immunostained for neurons – anti-βIII-tubulin (red) and astrocytes – anti-GFAP (green) and the general nuclear stain DAPI (blue). (b) Quantification of the percent area coverage of neurons with a circularity cutoff of 0.2 to eliminate cellular debris (mean ± SEM, n = 3 from two independent dissections). $^{**}p < 0.01$.

chamber (treatment *vs.* secondary) and microchannel height on the percent area covered by neurons ($p = 0.0095$). Analysis of the simple main effects (using Tukey's method to account for multiple comparisons) revealed a significantly reduced percent area coverage of neurons in the treatment chamber as compared to the secondary chamber in the devices with a 1.5 μm microchannel height ($p = 0.0057$). However, in the devices with 6 μm tall microchannels, we observed no significant difference ($p = 0.99$) in the neuron percent area coverage, indicating that the flow between the chambers was enough to "wash-out" the AraC from the treatment chamber preventing the neurotoxic effect. Additionally, we did not see a significant difference in the neuron coverage between the control chambers of the different devices ($p = 0.85$) indicating that reducing microchannel height does not negatively influence the fluidic isolation of the treatment chamber. We have observed similar results from established (DIV 14) cultures in devices with 1.5 μm tall channels, with severe neuronal death isolated to the treatment chamber following a 4 day excitotoxic challenge, whereas cultures in devices with 6 μm tall channels show no cell death in either chamber (Fig. S2†). These results indicate that reducing the height of the microchannels can significantly improve the fluidic properties of these devices, especially during extended treatment times. Furthermore, as half-media changes are required every 3–4 days to maintain the cultures, it is expected that the robust fluidic isolation observed in the 1.5 μm microchannel height devices can be maintained indefinitely, as the volume differential between the chambers can naturally be "reset" every 3–4 days. Finally, axonal growth into the channels likely further improves the fluidic isolation between the chambers by reducing the effective channel cross-section available for fluid flow, that is, increasing the hydraulic resistance.

An alternative method to reduce the flow between the chambers during fluidic isolation that has been used by some researchers is decreasing the volume difference between the control and treatment chambers.[14,15] While this method is effective in reducing the fluid flow by reducing the pressure differential, we found that this comes at the expense of fluidic isolation (Fig. S3†). We observed a similar reduction in fluid flow between the chambers by reducing the hydrostatic pressure differential in devices with 6 μm tall microchannels to ~0.71 mm as compared to devices with 1.5 μm tall microchannels with a more standard hydrostatic pressure differential (~2.83 mm). However, we also observed diffusion of dye molecules from the treatment chambers within the microchannels of the reduced-volume differential devices. This was not observed in devices with 1.5 μm or 6 μm tall microchannels that maintained the more standard hydrostatic pressure differential. This suggests that reducing microchannel height as opposed to reducing the hydrostatic pressure differential is the better solution to reduce the fluid flow through the microchannels when absolute fluidic isolation of the treatment chamber is critically important.

Influence of microchannel geometry of electrophysiological recording fidelity

Extracellular recording from neural cultures seeded onto MEAs in a well format have been widely used to study the development of neural circuit activity and responses to various pharmaceutical and pathological stimuli.[43] Similarly, MEAs can be integrated into microfluidic neural culture devices to record neural activity from synaptically-connected neural populations along with the interconnecting axons. While most research in this area has primarily been to demonstrate the ability to record large single unit recordings from axons within microchannel[44–46] or study the rate of action potential (AP) propagation along axons,[47,48] some researchers have begun to study the electrophysiological response of neurons cultured in these chambers to compartmentalized treatments[49,50] or develop directional neural networks.[51,52] For studying connected

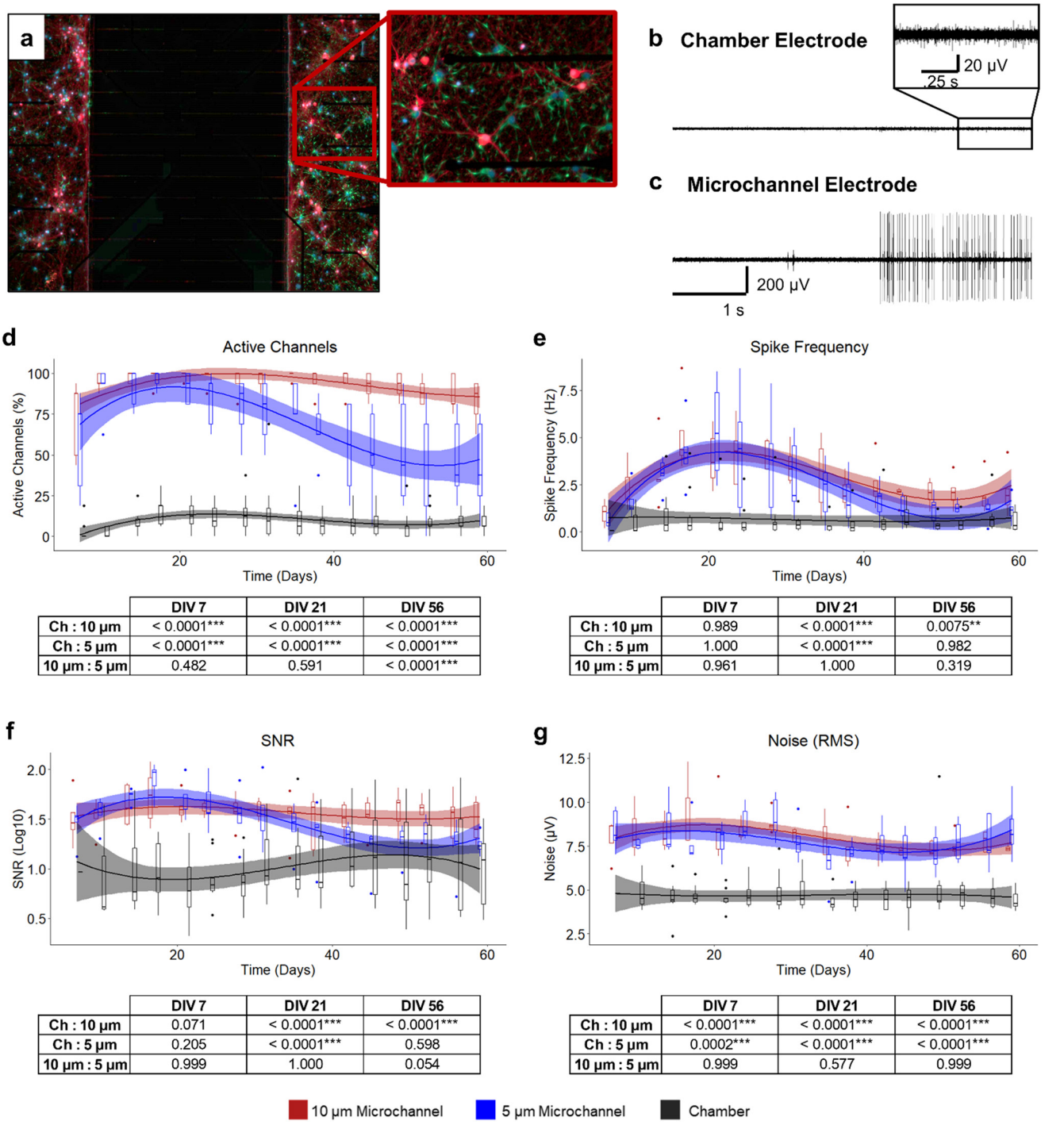

	DIV 7	DIV 21	DIV 56
Ch : 10 μm	< 0.0001***	< 0.0001***	< 0.0001***
Ch : 5 μm	< 0.0001***	< 0.0001***	< 0.0001***
10 μm : 5 μm	0.482	0.591	< 0.0001***

	DIV 7	DIV 21	DIV 56
Ch : 10 μm	0.989	< 0.0001***	0.0075**
Ch : 5 μm	1.000	< 0.0001***	0.982
10 μm : 5 μm	0.961	1.000	0.319

	DIV 7	DIV 21	DIV 56
Ch : 10 μm	0.071	< 0.0001***	< 0.0001***
Ch : 5 μm	0.205	< 0.0001***	0.598
10 μm : 5 μm	0.999	1.000	0.054

	DIV 7	DIV 21	DIV 56
Ch : 10 μm	< 0.0001***	< 0.0001***	< 0.0001***
Ch : 5 μm	0.0002***	< 0.0001***	< 0.0001***
10 μm : 5 μm	0.999	0.577	0.999

Fig. 6 (a) Representative fluorescence image of cortical cells cultured in the "MEA" style device for 59 DIV. The cultures were immunostained for neurons – anti-βIII-tubulin (red) and astrocytes – anti-GFAP (green) and the general nuclear stain DAPI (blue). Representative recordings taken at DIV 59 from an electrode placed (b) within the cell culture chamber and (c) under a microchannel. Comparisons of the (d) percent active channels, (e) spike frequency, (f) SNR, and (g) RMS noise from electrodes placed under 10 μm wide microchannels (red), 5 μm wide microchannels (blue), and within the cell culture chambers (black). The solid lines show the fitted linear mixed effects model (treating the individual devices as a random effect) with a b-spline basis. The shaded regions are the 95% confidence interval. The tables show the *p*-values comparing the estimated marginal means of the fitted curves at pre-determined timepoints (n = 5, from two independent dissections). $^{**}p < 0.01$, $^{***}p < 0.001$.

neural populations for longer durations (1+ month), it is necessary to determine the impact on microchannel geometry on electrophysiological recording fidelity. We seeded primary cortical cells at a concentration of 3×10^6 cells per mL and cultured them in "MEA" style devices integrated with a 32 channel MEA (16 electrodes were placed under the microchannels, and 8 were placed in each chamber) (Fig. 1c). Based on our previous results, we narrowed down the fabricated

devices to two microchannel geometries. All microchannels had lengths of 1000 μm to prevent astrocyte gap junction formation between the chambers and heights of 1.5 μm to minimize cell nuclei entering the chambers and improve fluidic isolation, informed by the studies above. The devices contained microchannels with either 5 μm or 10 μm channel widths, and the dimensions of the corresponding electrodes were adjusted to ensure a 400 μm^2 exposed electrode area. Additionally, the number of microchannels in the device was reduced from 101 to 25 and the surface area of each cell culture chamber was reduced to increase the likelihood of neurons attaching close to the chamber electrodes.

At DIV 59 the cultures maintained within the devices appeared healthy with robust neural processes and non-activated astrocyte morphologies[20] (Fig. 6a) and showed robust neural activity recorded from electrodes in both the chamber (Fig. 6b) and under the microchannels (Fig. 6c). Initially, the percentage of active electrodes (electrodes recording at least 10 spikes during the 10 min recording) increased for all electrode types (electrodes placed under 10 μm-wide microchannels, 5 μm-wide microchannels, and within cell culture chambers), with almost 100% active channels by DIV 17 for the microchannel electrodes (Fig. 6d). This increased percentage of active electrodes in the microchannels is likely due to the microchannels guiding the axons directly over the electrode sites, eliminating the stochastic effect of neuron–electrode proximity required for electrodes in the chambers. At early (DIV 7) and middle (DIV 21) timepoints when the cultures are maturing and reaching maturity respectively, there is no difference between the percentage of active channels in 10 μm and 5 μm wide microchannels ($p = 0.48$ at DIV 7 & $p = 0.59$ at DIV 21). However, the percentage of active electrodes begin to decline at a much more rapid rate for 5 μm-wide microchannel electrodes as compared to electrodes under the 10 μm-wide channels, and by DIV 56 we observe a significant difference in the percent active electrodes ($p < 0.0001$). The decline in the number of active channels over time is not unexpected as it has been shown that the overall health of primary cortical cultures begins to decline around 28–35 DIV.[21,53] We expect that over time the axons in the microchannel may begin to deteriorate as the overall health of the neuron declines, and as the 10 μm-wide microchannels contain more axons, this decrease is less pronounced as recording neural activity from only a single healthy axon is required to classify an electrode as active.

We see a similar relationship between electrode types when comparing changes in spike frequency (Fig. 6e). Once again, for microchannels, there is an initial increase in firing rate as the culture matures followed by a decrease as the culture ages. The significant differences in estimated marginal means at DIV 21 between the microchannel and chamber electrodes ($p < 0.0001$ for both 5 μm and 10 μm microchannels) can be attributed to recording from multiple axons within the microchannels. This also supports previous studies that show the AP from one axon within a microchannel does not depolarize other axons within the microchannel.[45,47] Unlike the number of active channels, there was no difference in firing rate between the 5 μm and 10 μm-wide microchannels at DIV 56 ($p = 0.32$). This difference can partially be attributed to the fact that non-active channels were excluded from the spike frequency analysis, and therefore contributions from rapidly degrading axons were not included in the analysis. Unlike the recordings from the microchannels, the firing rate of neurons in the chamber was relatively stable following the initial rise as the culture matured. This indicates that the neurons in the culture chambers may remain relatively healthy, but over time a portion of the axons within the microchannels begin the degrade.

We report significant increases in SNR (Fig. 6f) and noise (Fig. 6g) from electrodes within the microchannels as compared to those in the cell culture chambers. This is in line with previous reports showing increased SNR and noise floors from electrodes placed within microchannels.[45–47] The increase in noise can largely be attributed to the increase in electrode impedance due to the added electrical resistance along the length of the microchannel.[45] Similarly the increased resistance in the microchannel due to the spatial confinement leads to an increase in the spike amplitude.[46] Additionally, large numbers of neurites and astrocytes can block both sides of the microchannels essentially creating a high-resistance seal, which can dramatically increase the spike amplitude and lead to the much larger SNR seen in the microchannels (with a roughly order of magnitude difference at DIV 21).[46] Interestingly, we saw a decrease in SNR over time in the 5 μm microchannels that was not observed in the 10 μm microchannels. As the microchannel geometries do not change over the course of the experiment, this may be attributed to a loss of the high-resistance seal in the 5 μm microchannels.

We also compared a number of different electrophysiological features (percentage of spikes in bursts, within burst ISI, and burst duration) to assess culture maturation and stability over time (Fig. 7a–c). As expected, we see an increase in the percentage of spikes in bursts across all electrode types as the cultures mature. Additionally, over time we see a similar change in the percent of spikes in bursts as with the firing rate. Within microchannels, the percentage of spikes in bursts begins to decrease, presumably as some axons within the microchannels begin to degrade. In contrast, within the chamber, the values remain relatively constant, again suggesting that the neurons in the culture chambers remain healthy over the extended culture times. We also observe minimal changes over time for the within-burst ISI and burst duration, which also suggests that the cultures are healthy over the 59 DIV.

Finally, we compared the overall synchrony in devices with 5 μm and 10 μm-wide channels to assess the network development and stability over time (Fig. 7d). We calculated the overall synchrony by comparing the dissimilarity of the spike trains of active channels using the SPIKE-distance method[25,26] (with values closer to 1 indicating higher levels of synchronization between the spike trains of active channels). While we observed an increase in synchrony for both devices as the cultures matured, the devices with 10 μm-wide channels reached a higher degree of

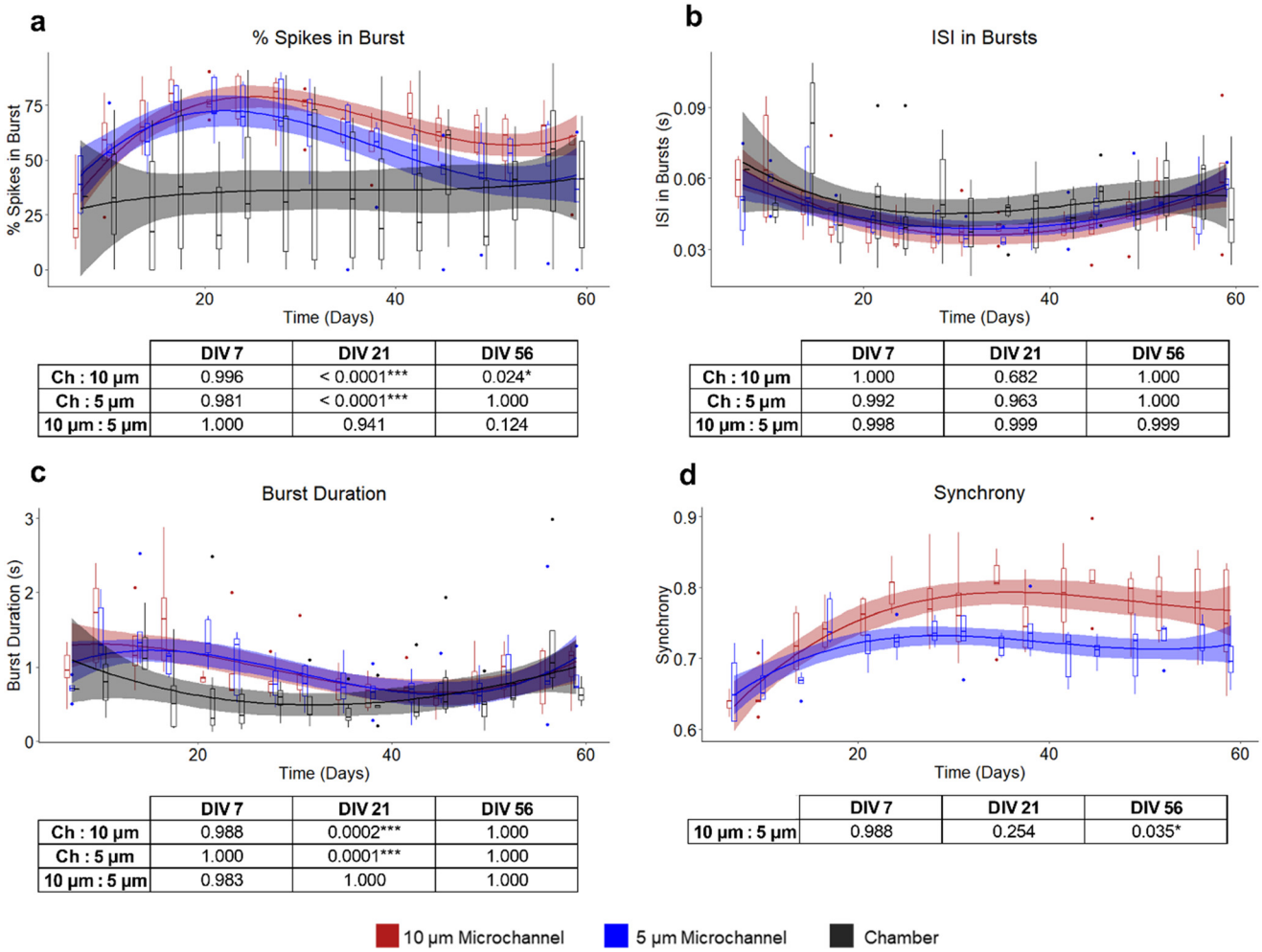

	DIV 7	DIV 21	DIV 56
Ch : 10 µm	0.996	< 0.0001***	0.024*
Ch : 5 µm	0.981	< 0.0001***	1.000
10 µm : 5 µm	1.000	0.941	0.124

	DIV 7	DIV 21	DIV 56
Ch : 10 µm	1.000	0.682	1.000
Ch : 5 µm	0.992	0.963	1.000
10 µm : 5 µm	0.998	0.999	0.999

	DIV 7	DIV 21	DIV 56
Ch : 10 µm	0.988	0.0002***	1.000
Ch : 5 µm	1.000	0.0001***	1.000
10 µm : 5 µm	0.983	1.000	1.000

	DIV 7	DIV 21	DIV 56
10 µm : 5 µm	0.988	0.254	0.035*

Fig. 7 Comparisons of the (a) percentage of total spikes in bursts, (b) within-burst ISI, and (c) burst duration from electrodes placed under 10 µm wide microchannels (red), 5 µm wide microchannels (blue), and within the cell culture chambers (black). (d) Comparing the overall synchrony in devices with 10 µm-wide microchannels (red) and 5 µm-wide microchannels (blue). The solid lines show the fitted linear mixed effects model (treating the individual devices as a random effect) with a b-spline basis. The shaded regions are the 95% confidence interval. The tables show the *p*-values comparing the estimated marginal means of the fitted curves at pre-determined timepoints (n = 5, from two independent dissections). *$p < 0.05$, **$p < 0.01$, ***$p < 0.001$.

synchronization (p = 0.035 at DIV 56). This is presumably due to the increased number of axons crossing through the wider microchannels and form a more robust network between the two separated chambers. We also observed that for both devices the synchrony plateaued following the initial rise, suggesting that the network is stable over the extended culture times. Overall, these results suggest that increasing microchannel width may improve network formation between the microchannels and improve electrophysiological recording fidelity within the microchannels.

Conclusions

In this study, we have demonstrated the significant impact of small changes in microchannel geometry can have on the overall device functionality of commonly used microfluidic neural culture platforms. In particular, we studied how microchannel geometry influenced the cellular confinement, axon crossings, fluidic properties, and electrophysiological recording fidelity when using these devices. It is important to note that all experiments in this study were performed using cortical cells from neonatal rats. While the size distribution of neurons and astrocytes in mice and rats are similar, the axon diameter and overall astrocyte size of human cells tends to skew slightly larger.[19,54–56] As the size difference between neuronal cells from rodents and humans are relatively minimal (for example over 95% axons from rat,[19] mouse,[54] and human[56] cortical neurons are less than 1.5 µm) we do not expect the cell source to significantly impact the results from this study. Additionally, as both human neurons and astrocytes are larger than their rodent counterparts, the overall conclusions drawn from this study should remain applicable across species. Below, we describe how each design factor can influence device functionality and summarize general design rules for different experimental objectives (Fig. 8).

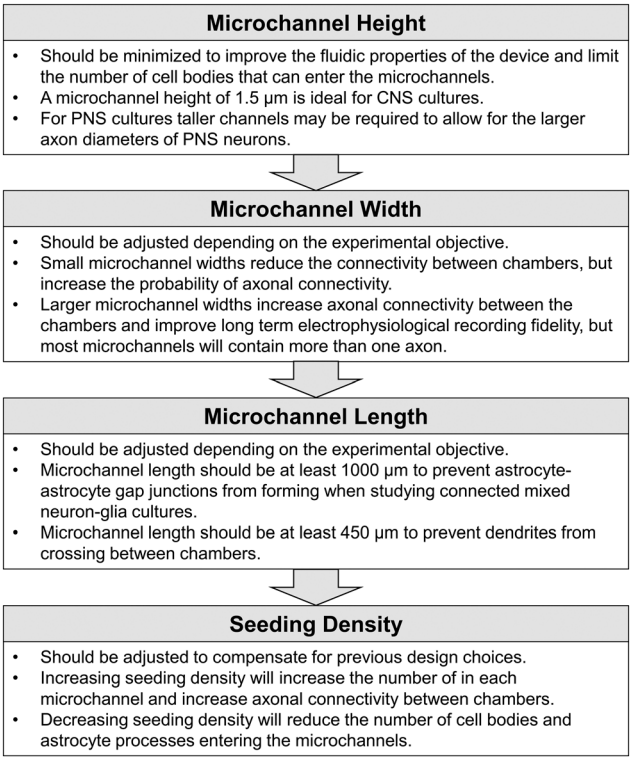

Fig. 8 A summary of general step-wise design rules for different experimental objectives.

i) Microchannel height

It is best to keep microchannel height as small as possible, ideally around 1.5 μm. Reducing microchannel heights to this value significantly reduces the number of cell bodies that can enter the microchannels (improving cellular confinement) while minimally impacting the ability for axons to enter the channels. Additionally, there is a significant reduction in the volumetric flow rate through the microchannels when a hydrostatic pressure differential is maintained. This is especially critical for long-term studies, where fluid flow between the chambers can significantly alter the concentration of soluble factors added to the fluidically isolated chamber. In general, we do not recommend increasing microchannel height above 1.5 μm, with the exception that if peripheral neurons are being cultured taller microchannels may be required to accommodate the larger axon diameters. In this case the initial seeding density should be reduced to minimize the number of cells that enter the microchannels, and treatment times should be kept to a minimum to minimize changes in the effector molecule concentration.

ii) Microchannel length

For long-term experiments studying connected neural populations, in which both neurons and astrocytes will be added to both sides of the microchannels, it is important that the microchannels are at least 1000 μm in length to prevent the formation of astrocyte–astrocyte gap junctions within the microchannels. For experiments in which cells are cultured on only one side of the microchannels or when only neurons are being cultured, the previous recommended length of 450–500 μm should be used to prevent dendrites from crossing through the channels.[4]

iii) Microchannel width

For extended studies of connected neural populations, we suggest a microchannel width of at least 5 μm to ensure robust connectivity between the chambers. Increasing microchannel width beyond 5 μm can improve the long-term electrophysiological recording fidelity, at the cost of increasing the number of axons in each microchannel. If robust synaptic connectivity between the chambers is desired, increasing the number of axons in each microchannel is beneficial and there is little to no drawback from increasing microchannel width. If the experiment requires a single axon to be present in each microchannel (*i.e.*, single axon imaging or electrophysiological recording studies) reducing the microchannel width down to 2 μm may be worthwhile. If this is the case, increasing the initial seeding density can be used to counteract the reduced axon crossings and improve the overall connectivity between the chambers.

iv) Initial seeding density

The initial seeding density can largely be used as a tool or countermeasure to reduce some of the negative side effects of altering microchannel geometries. Increasing seeding density can be used to increase the number of axons crossing the microchannels when using devices with small microchannel widths or very long microchannel lengths. Alternatively, reducing the seeding density can improve the cellular confinement of devices with large microchannel heights. Additionally, reducing initial seeding density can substantially reduce the number of astrocyte processes within the microchannels.

Author contributions

NG and ES designed the experiments. NG performed device fabrication, cell culture, electrophysiological recordings, imaging, and data analysis and wrote the main manuscript text. GG contributed to the development and fabrication of microfluidic devices and microelectrode arrays, and data analysis. FDCS contributed to the development of the cell culture. AG contributed to electrophysiological data analysis. ES and PJL contributed to the interpretation of experimental results and edited the manuscript. All authors read and approved the final manuscript.

Conflicts of interest

The authors declare no conflicts of interest.

Acknowledgements

We gratefully acknowledge the support from the National Institutes of Health *via* NINDS/NIA R03-NS118156, NIBIB R21-EB024635, and NCCIH R21-AT010933, and from the National Science Foundation *via* CBET-1454426 and DMR-2003849. NG was partially supported by the UC Davis Biotechnology Training Program award. This project benefited from the resources of the MIND Institute IDDRC Core services (NICHD P50-HD103526) and University of California, Davis – Center for Nano/Micro-Manufacturing facility.

References

1 R. Yuste, *Nat. Rev. Neurosci.*, 2015, **16**, 487–497.
2 D. E. Pankevich, B. M. Altevogt, J. Dunlop, F. H. Gage and S. E. Hyman, *Neuron*, 2014, **84**, 546–553.
3 Y. Berdichevsky, K. J. Staley and M. L. Yarmush, *Lab Chip*, 2010, **10**(8), 999–1004.
4 A. M. Taylor, S. W. Rhee, C. H. Tu, D. H. Cribbs, C. W. Cotman and N. L. Jeon, *Langmuir*, 2003, **19**, 1551–1556.
5 A. M. Taylor, M. Blurton-Jones, S. W. Rhee, D. H. Cribbs, C. W. Cotman and N. L. Jeon, *Nat. Methods*, 2005, **2**, 599–605.
6 A. Virlogeux, E. Moutaux, W. Christaller, A. Genoux, J. Bruyère, E. Fino, B. Charlot, M. Cazorla and F. Saudou, *Cell Rep.*, 2018, **22**, 110–122.
7 J. M. Peyrin, B. Deleglise, L. Saias, M. Vignes, P. Gougis, S. Magnifico, S. Betuing, M. Pietri, J. Caboche, P. Vanhoutte, J. L. Viovy and B. Brugg, *Lab Chip*, 2011, **11**, 3663–3673.
8 A. Iannielli, G. S. Ugolini, C. Cordiglieri, T. Cabassi, M. Rasponi, V. Broccoli, A. Iannielli, G. S. Ugolini, C. Cordiglieri, S. Bido, A. Rubio, G. Colasante, M. Valtorta, T. Cabassi, M. Rasponi and V. Broccoli, *Cell Rep.*, 2019, **29**, 4646–4656.
9 J. C. Polanco, C. Li, N. Durisic, R. Sullivan and J. Götz, *Acta Neuropathol. Commun.*, 2018, **6**, 10.
10 L. Urrea, M. Segura-Feliu, M. Masuda-Suzukake, A. Hervera, L. Pedraz, J. M. G. Aznar, M. Vila, J. Samitier, E. Torrents, I. Ferrer, R. Gavín, M. Hagesawa and J. A. del Río, *Mol. Neurobiol.*, 2018, **55**, 1847–1860.
11 M. Brahic, L. Bousset, G. Bieri, R. Melki and A. D. Gitler, *Acta Neuropathol.*, 2016, **131**, 539–548.
12 S. Akira and K. Takeda, *Nat. Rev. Immunol.*, 2004, **4**, 499–511.
13 S. Takeda, S. Wegmann, H. Cho, S. L. Devos, C. Commins, A. D. Roe and S. B. Nicholls, *et al.*, *Nat. Commun.*, 2015, **6**(1), 1–15.
14 H. L. Song, S. Shim, D. H. Kim, S. H. Won, S. Joo, S. Kim, N. L. Jeon and S. Y. Yoon, *Ann. Neurol.*, 2014, **75**, 88–97.
15 A. J. Samson, G. Robertson, M. Zagnoni and C. N. Connolly, *Sci. Rep.*, 2016, **6**, 1–11.
16 K. A. Southam, A. E. King, C. A. Blizzard, G. H. McCormack and T. C. Dickson, *J. Neurosci. Methods*, 2013, **218**, 164–169.
17 J. Bellmann, R. Y. Goswami, S. Girardo, N. Rein, Z. Hosseinzadeh, M. R. Hicks, V. Busskamp, A. D. Pyle, C. Werner and J. Sterneckert, *Biomaterials*, 2019, **225**, 119537.
18 J. C. Fiala and K. M. Harris, in *Dendrites 2*, 1999, pp. 1–11.
19 G. Partadiredja, R. Miller and D. E. Oorschot, *J. Neurocytol.*, 2003, **32**, 1165–1179.
20 N. Goshi, R. K. Morgan, P. J. Lein and E. Seker, *J. Neuroinflammation*, 2020, **17**, 1–16.
21 H. A. Enright, D. Lam, A. Sebastian, A. P. Sales, J. Cadena, N. R. Hum, J. J. Osburn, S. K. G. Peters, B. Petkus, D. A. Soscia, K. S. Kulp, G. G. Loots, E. K. Wheeler and N. O. Fischer, *Sci. Rep.*, 2020, **10**, 1–14.
22 V. M. Tiryaki, V. M. Ayres, I. Ahmed and D. I. Shreiber, *Nanomedicine*, 2015, **10**, 529–545.
23 G. Robertson, T. J. Bushell and M. Zagnoni, *Integr. Biol.*, 2014, **6**, 636–644.
24 G. A. Wayman, D. D. Bose, D. Yang, A. Lesiak, D. Bruun, S. Impey, V. Ledoux, I. N. Pessah and P. J. Lein, *Environ. Health Perspect.*, 2012, **120**, 1003–1009.
25 T. Kreuz, D. Chicharro, C. Houghton, R. G. Andrzejak and F. Mormann, *J. Neurophysiol.*, 2013, **109**, 1457–1472.
26 M. Mulansky and T. Kreuz, *SoftwareX*, 2016, **5**, 183–189.
27 P. Charlesworth, E. Cotterill, A. Morton, S. G. N. Grant and S. J. Eglen, *Neural Dev.*, 2015, **10**, 1–10.
28 P. Froeter, Y. Huang, O. V. Cangellaris, W. Huang, E. W. Dent, M. U. Gillette, J. C. Williams and X. Li, *ACS Nano*, 2014, **8**, 11108–11117.
29 L. Vitzthum, X. Chen, D. B. Kintner, Y. Huang, S. Y. Chiu, J. Williams and D. Sun, *Integr. Biol.*, 2010, **2**, 58–64.
30 R. K. Pirlo, A. J. Sweeney, B. R. Ringeisen, M. Kindy and B. Z. Gao, *Biomicrofluidics*, 2011, **5**(1), 013408.
31 L. Li, L. Ren, W. Liu, J. C. Wang, Y. Wang, Q. Tu, J. Xu, R. Liu, Y. Zhang, M. S. Yuan, T. Li and J. Wang, *Anal. Chem.*, 2012, **84**, 6444–6453.
32 A. Bastiaens, R. Sabahi-Kaviani and R. Luttge, *Front. Neurosci.*, 2020, **14**, 1–11.
33 M. T. Doolin, T. S. Ornstein and K. M. Stroka, *Cells*, 2019, **8**, 1–17.
34 M. Le Berre, J. Aubertin and M. Piel, *Integr. Biol.*, 2012, **4**, 1406–1414.
35 T. N. Behar, S. V. Smith, R. T. Kennedy, J. M. Mckenzi, I. Maric and J. L. Barker, *Cereb. Cortex*, 2001, **11**, 744–753.
36 M. A. Haas, J. A. Chuckowree, R. S. Chung, J. C. Vickers and T. C. Dickson, *Cell Motil. Cytoskeleton*, 2007, **64**, 274–287.
37 E. A. Lepekhin, C. Eliasson, C. H. Berthold, V. Berezin, E. Bock and M. Pekny, *J. Neurochem.*, 2001, **79**, 617–625.
38 D. Majumdar, Y. Gao, D. Li and D. J. Webb, *J. Neurosci. Methods*, 2011, **196**, 38–44.
39 J. Park, H. Koito, J. Li and A. Han, *Lab Chip*, 2012, **12**, 3296–3304.
40 S. Hosmane, I. H. Yang, A. Ruffin, N. Thakor and A. Venkatesan, *Lab Chip*, 2010, **10**, 741–747.
41 H. U. Lee, S. Nag, A. Blasiak, Y. Jin, N. Thakor and I. H. Yang, *ACS Chem. Neurosci.*, 2016, **7**, 1317–1324.
42 D. P. Martin, T. L. Wallace and E. M. Johnson, *J. Neurosci.*, 1990, **10**, 184–193.
43 M. V. Accardi, M. K. Pugsley, R. Forster, E. Troncy, H. Huang and S. Authier, *J. Pharmacol. Toxicol. Methods*, 2016, **81**, 47–59.

44 N. Hong, S. Joo and Y. Nam, *IEEE Trans. Biomed. Eng.*, 2017, **64**, 492–498.
45 L. Pan, S. Alagapan, E. Franca, T. Demarse, G. J. Brewer and B. C. Wheeler, *IEEE Trans. Neural Syst. Rehabilitation Eng.*, 2014, **22**, 453–459.
46 L. Wang, M. Riss, J. O. Buitrago and E. Claverol-tinturé, *Journal of Neural Engineering*, 2012, **9**(2), 026010.
47 M. K. Lewandowska, D. J. Bakkum, S. B. Rompani and A. Hierlemann, *PLoS One*, 2015, **10**, 1–24.
48 K. Shimba, K. Sakai, K. Arimatsu, K. Kotani and Y. Jimbo, *Int. IEEE/EMBS Conf. Neural Eng.*, 2013, 945–948.
49 R. Habibey, A. Golabchi, S. Latifi, F. Difato and A. Blau, *Lab Chip*, 2015, **15**, 4578–4590.
50 M. K. Lewandowska, M. Radivojević, D. Jäckel, J. Müller and A. R. Hierlemann, *Front. Neurosci.*, 2016, **10**, 83.
51 G. J. Brewer, M. D. Boehler, S. Leondopulos, L. Pan, S. Alagapan, T. B. DeMarse and B. C. Wheeler, *Front. Neural Circuits*, 2013, **7**, 1–8.
52 T. Honegger, M. A. Scott, M. F. Yanik and J. Voldman, *Lab Chip*, 2013, **13**, 589–598.
53 C. A. R. Chapman, L. Wang, H. Chen, J. Garrison, P. J. Lein and E. Seker, *Adv. Funct. Mater.*, 2016, **1604631**, 1604631.
54 C. L. Call and D. E. Bergles, *Nat. Commun.*, 2021, **12**(1), 1–15.
55 B. Zhou, Y. X. Zuo and R. T. Jiang, *CNS Neurosci. Ther.*, 2019, **25**, 665–673.
56 D. Liewald, R. Miller, N. Logothetis, H. J. Wagner and A. Schüz, *Biol. Cybern.*, 2014, **108**, 541–557.